

Structures, charge density wave, and superconductivity of noncentrosymmetric $4H_a$ -NbSe₂Menghu Zhou ^{1,*}, Yadong Gu,¹ Shunli Ni,² Binbin Ruan,¹ Qiaoyu Liu,^{1,3} Qingsong Yang ^{1,3}, Lewei Chen,^{1,3} Junkun Yi,^{1,3} Yunqing Shi,^{1,3} Genfu Chen,^{1,3} and Zhian Ren ^{1,3,†}¹Beijing National Laboratory for Condensed Matter Physics, Institute of Physics, Chinese Academy of Sciences, Beijing 100190, China²School of Mathematics and Physics, University of South China, Hengyang 421001, China³School of Physical Sciences, University of Chinese Academy of Sciences, Beijing 100049, China

(Received 25 September 2023; revised 5 December 2023; accepted 6 December 2023; published 27 December 2023)

We report the crystal and electronic structures, charge density wave (CDW), and superconductivity of polycrystalline $4H_a$ -NbSe₂ studied by x-ray diffraction, *ab initio* calculations, electrical resistivity, magnetization, and specific heat. $4H_a$ -NbSe₂ has no central inversion symmetry (space group $P-6m2$), and the stacking-fault structure was observed in the crystal lattice. The weak CDW transition at $T_{CDW} \sim 43$ K thermodynamically is of second order. $4H_a$ -NbSe₂ has a superconducting critical temperature $T_c \sim 6.4$ K, which is a moderately coupled BCS superconductor with two-gap $s + s$ -wave-like pairing. The upper critical field $\mu_0 H_{c2}(0)$ is as high as 26.5 T which far exceeds the Pauli paramagnetic limit and this violation is mostly attributed to the breaking of the central inversion symmetry. Second magnetization peaks can be observed in the system with weak flux pinning. Electronic structure calculations reveal that the Nb $4d$ orbitals dominate the bands near the Fermi level with different degree of hybridization between the Nb $4d$ and Se $4p$ orbitals in $2H$ - and $4H_a$ -NbSe₂, and the band structures of $4H_a$ -NbSe₂ favor a higher T_{CDW} . The higher T_{CDW} but lower T_c compared to $2H$ -NbSe₂ leads us to conclude that the two collective electronic states are competitive on the Fermi surface in this system. The large $\mu_0 H_{c2}(0)$ derived from $4H_a$ -NbSe₂ is expected to stimulate the explorations for high-field superconductor applications from a noncentrosymmetric structural strategy.

DOI: [10.1103/PhysRevB.108.224518](https://doi.org/10.1103/PhysRevB.108.224518)**I. INTRODUCTION**

Quasi-two-dimensional transition-metal dichalcogenides (TMDs) have received great interest due to hosting polymorphism, for example $1T$, $2H$, $3R$, and $4H$ polytypes, and exhibiting rich electronic properties, such as Mott state, possible spin liquid state, charge density wave (CDW), and superconductivity (SC) [1–11]. NbSe₂, one of the most famous TMD compounds, has eight structural modifications reported up to now [12,13]. There has been no experimental report about bulk $1T$ -NbSe₂ up to now, and recent electronic-structure calculations indicate a band gap ~ 0.02 eV in bulk CDW $1T$ -NbSe₂ by considering the interlayer antiferromagnetic ordering and a strong dependence of electronic structures on stacking configurations [14]. Monolayer $1T$ -NbSe₂ on bilayer graphene with Star-of-David CDW structure was found as a Mott insulator with a gap ~ 0.4 eV [15,16]. $2H$ -NbSe₂ ($2H_a$) with superconducting and CDW transition temperatures, respectively, at $T_c \sim 7.4$ K and $T_{CDW} \sim 33$ K, has been extensively investigated. The origin of the CDW instability in the $2H$ phase is believed to be primarily driven by momentum-dependent electron-phonon coupling (EPC) rather than Fermi-surface nesting and saddle-point mechanisms [17–20]. The superconductivity in $2H$ -NbSe₂ exhibits a multigap feature [21–24]. It is curious that the SC and CDW

orders in $2H$ -NbSe₂ are usually suppressed concurrently by impurity doping. The reason for this remains an open question and the EPC may play an important role in the anomalous behavior. Besides, the weak CDW transition is very sensitive to native defects, such as vacancies, intercalants, dislocations, and so on [25]. The CDW order was strongly enhanced and Ising superconductivity was realized in monolayer NbSe₂ ($1H$ -NbSe₂) [26,27]. However, the study on the $4H$ polymorph is scarce, though several $4H$ forms, such as $4H_a$, $4H_{dl}$, and $4H_{dl}$, have been reported in the literature [12]. Noncentrosymmetric $4H_a$ -NbSe₂, as a member of CDWs in TMDs, has received less attention. The SC and CDW with $T_c \sim 6.5$ K and $T_{CDW} \sim 42$ K were only revealed by very few sporadic experiments [28–31]. Only a simple H_{c2} - T phase diagram was reported and the nature of the CDW transition has not been identified yet [30]. μSR experiment indicates that the superfluid density in $4H$ -NbSe₂ scales linearly with T_c and could be described by a two-gap $s+s$ -wave picture [31].

The lack of systematic electrical, magnetic, and specific-heat data for $4H_a$ -NbSe₂ prevents one from gaining more insight into the superconducting state and from revealing the nature of the CDW transition. In this paper, the properties of the CDW transition and SC state were systematically characterized on $4H_a$ -NbSe₂ polycrystalline sample by electrical resistivity, magnetization, and specific-heat measurements. The reasons for choosing polycrystalline sample as the research object were as follows: (1) in most cases the CDW transition in $4H_a$ -NbSe₂ could not be observed in single crystals in macroscopic measurements due to native defects

*Corresponding author: zhoumenghu@iphy.ac.cn

†Corresponding author: renzhian@iphy.ac.cn

produced by quenching the sample from high temperature (900 °C) to room temperature, and (2) $4H_a$ -NbSe₂ is usually symbiotic with $2H$ -NbSe₂ due to the incomplete quenching in large-size single crystals. The crystal structure was studied by x-ray diffraction and the electronic structures were evaluated by *ab initio* calculations. It was revealed that the CDW transition is second order in nature. Superconducting state was analyzed, which indicated that $4H_a$ -NbSe₂ is an intermediately coupled *s*-wave superconductor with possible two-gap pairing feature and with a high upper critical field $\mu_0 H_{c2}$ violating the Pauli limit. The reverse relation of SC and CDW orders in $2H$ - and $4H_a$ -NbSe₂ revealed a competition between the two electronic states in NbSe₂ system.

II. EXPERIMENTAL DETAILS

Polycrystalline $4H_a$ -NbSe₂ sample was prepared by solid-state reaction from stoichiometric amount of Nb (99.99%) and Se (99.999%) powders. The starting materials were fully mixed and pressed into pellets, which were sealed in an evacuated silica ampoule and then heated at 900 °C for 2 days. The as-prepared sample with metallic luster was ground, pelletized, and heated at 900 °C under vacuum for 3 days. Finally, the bulk polycrystalline sample was obtained by a quick quenching process in the air.

The morphology and composition for the pristine surface of the bulk specimen were analyzed by using a Phenom scanning electron microscope (SEM) equipped with an energy-dispersive x-ray spectrometer (EDS). X-ray diffraction (XRD) patterns were recorded at room temperature on a PANalytical x-ray diffractometer with Cu- K_α radiation. The crystal structure was refined by the Rietveld method (GSAS software) [32]. *Ab initio* calculations were performed with the QUANTUM ESPRESSO package by using the generalized gradient approximation (GGA) of Perdew-Burke-Ernzerhof (PBE) exchange-correlation functionals and ultrasoft pseudopotentials [33–35]. Electrical resistivity and heat-capacity measurements were carried out on a Quantum Design physical property measurement system (PPMS-16T) by using the four-probe method and thermal-relaxation method, respectively. Magnetization was measured on a Quantum Design vibrating sample magnetometer (MPMS-VSM).

III. RESULTS AND DISCUSSION

A. Crystal structure

The SEM micrograph for the pristine surface of the bulk sample in the inset of Fig. 1(a) shows that the crystal possesses hexagonal morphology and layered structure with in-plane grain size of about 50 μm . The *c*-axis preferred orientation frequently occurring in layered TMDs can be clearly observed in the bulk $4H_a$ -NbSe₂ as revealed by SEM image [the inset in Fig. 1(a)] and XRD pattern [the upper pattern in Fig. 1(b)]. EDS analysis on multiple points obtained the average atomic ratio of Nb and Se as 0.97(6):2, which is close to the nominal/ideal composition. The elemental mappings show the homogeneity of the sample. The phase purity was checked by XRD, revealing the single $4H_a$ -NbSe₂ without intergrowth with the $2H$ -polytype. This indicates the high quality of the sample. As shown in the inset of Fig. 1(b), the weakening

TABLE I. Refined crystallographic data for $4H_a$ -NbSe₂ determined at room temperature together with the refinement residuals.

Chemical formula		$4H_a$ -NbSe ₂			
Space group		$P-6m2$ (No. 187)			
Cell content <i>Z</i>		4			
<i>a</i> (Å)		3.4432(8)			
<i>c</i> (Å)		25.2294(7)			
Cell volume (Å ³)		259.04(2)			
R_p		4.64%			
R_{wp}		7.42%			

Atom	Wyckoff letter	<i>x</i>	<i>y</i>	<i>z</i>	Occ.
Nb1	1 <i>a</i>	0	0	0	1.0
Nb2	2 <i>g</i>	0	0	0.2492(6)	1.0
Nb3	1 <i>f</i>	2/3	1/3	1/2	1.0
Se1	2 <i>i</i>	2/3	1/3	0.0664(7)	1.0
Se2	2 <i>h</i>	1/3	2/3	0.1846(8)	1.0
Se3	2 <i>h</i>	1/3	2/3	0.3210(3)	1.0
Se4	2 <i>g</i>	0	0	0.4303(1)	1.0

and broadening of the reflections with index (10*l*) is a typical feature of randomly stacked structure that may cause an enhanced anisotropy of the quasi-2D compound [36–39]. Stacking-fault structure is common in TMDs with a noninteger number of valence electrons and could be described by the mixed-layer structure model [37,38]. The crystal structure was refined by the Rietveld method based on the XRD data of the powder with a slightly weaker preferred orientation [the lower pattern in Fig. 1(b)]. The refinement profiles are plotted in Fig. 1(c), and the structural parameters and refinement residuals are listed in Table I. The structural motif in both $2H_a$ - and $4H_a$ -NbSe₂ is the NbSe₆ trigonal prism illustrated in the inset of Fig. 1(c); they contain, respectively, two and four NbSe₆ layers in the unit cell. The axial ratios *c/a* for $2H_a$ - and $4H_a$ -NbSe₂ are, respectively, 3.64 and 7.34, indicating higher anisotropy of the $4H_a$ polymorph and thus enhanced two dimensionality. The $4H_a$ could appear as a consequence of periodic stacking fault in the $2H_a$. In the $4H_a$ phase, the first two layers (layer 1 and layer 2) stack in $2H$ -form, while the third layer (layer 3) translates by a vector ($2a/3 + b/3$) within the *ab* plane relative to layer 2. This thus leads to a reduced symmetry from $P6_3/mmc$ ($2H_a$) to $P-6m2$ ($4H_a$), respectively, with and without central inversion symmetry.

B. CDW transition

Temperature-dependent resistivity $\rho(T)$ in Fig. 2(a) displays a metallic behaviour. The observed curvature of the experimental $\rho(T)$ above the CDW transition ($T > 43$ K) cannot be described by the simple Bloch-Grüneisen (BG) relation [green line in Fig. 2(a)] expected for low *d*-band density-of-states metals. The Bloch-Grüneisen-Mott (BGM) formula taking *s-d* interband scattering [40] into account is introduced to fit the data:

$$\rho(T) = \rho_0 + A \left(\frac{T}{\Theta_R} \right)^5 \int_0^{\Theta_R/T} \frac{x^5}{(e^x - 1)(1 - e^{-x})} dx - \alpha T^3, \quad (1)$$

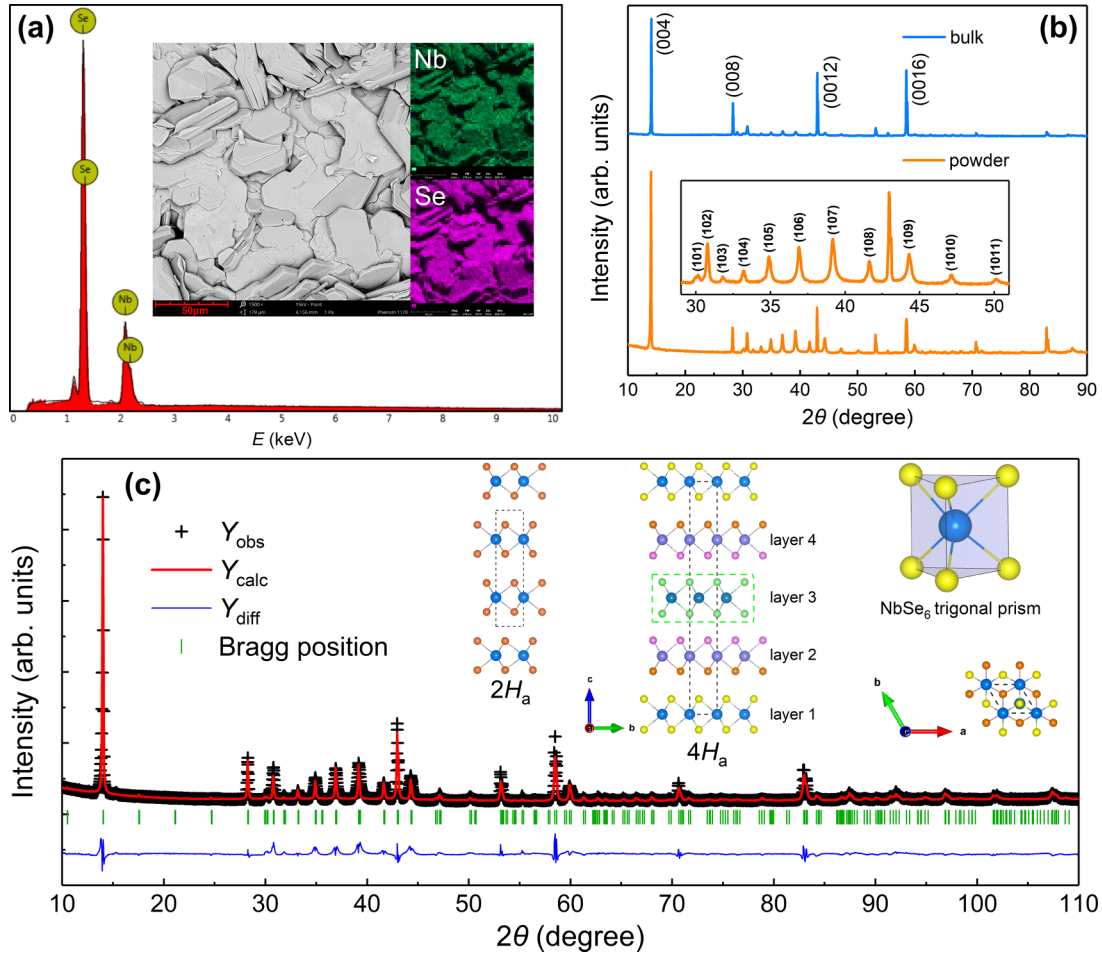


FIG. 1. (a) EDS spectrum for the pristine surface of $4H_a$ -NbSe₂ bulk sample; the inset shows the SEM image and elemental mappings. (b) XRD patterns for the bulk and powder samples with partial reflections indexed. The inset displays an enlarged view of the pattern for the powder sample. (c) Rietveld refinement profiles for $4H_a$ -NbSe₂. The inset presents the crystal structures of the $2H_a$ and $4H_a$ phases, and the structural motif NbSe₆ trigonal prism. The bigger balls represent Nb atoms and the smaller ones denote Se atoms.

where ρ_0 is the T -independent residual resistivity, the second term represents a T -dependent resistivity caused by electron-phonon scattering. A is a constant related to EPC strength, and Θ_R is the transport Debye temperature. The T^3 term is namely due to the Mott s - d interband scattering and α is the Mott coefficient. A least-square fitting yields the parameters in Eq. (1): $\rho_0 = 0.11(4)$ m Ω cm, $A = 1.8(1)$ m Ω cm, $\Theta_R = 145.1(8)$ K, and $\alpha = 6.4(3) \times 10^{-9}$ m Ω cm K⁻³. The BGM model [orange line in Fig. 2(a)] gives a good explanation, which indicates that $4H$ -NbSe₂ should be viewed as a “transition metal” with significant d -band density of states. Density-functional (DFT) calculations show the Nb $4d_{xy}/d_{x^2-y^2}$ and Se $4p_z$ -dominated Fermi surface, which suggests the validity of the BGM formula including s - d interband transitions. Resistivity measurement gives Θ_R smaller than Θ_D (214.8 K) obtained by specific heat from 1.8 to 10 K. Note that Debye temperature is temperature dependent. Θ_R determined in the temperature range $\Theta_R/3$ to Θ_R (and higher) is generally comparable to Θ_D for range $\Theta_D/2$ to Θ_D but smaller than Θ_D obtained from low-temperature ($T < \Theta_D/10$) Debye approximation in transition metals. This difference may be originated from Umklapp processes or electron-electron correlation; the latter is revealed by DFT calculations where

the p - d orbital hybridization can be obviously observed in energy bands. Residual resistivity ratio RRR is defined as $\rho(300 \text{ K})/\rho(T_c)$, which is calculated to be 8.6 for the polycrystalline bulk. Such RRR value is relatively large in polycrystalline TMDs. This may play a crucial role in observing the weak CDW transition which highly depends on the sample quality in the NbSe₂ system. Magnetic susceptibility (χ) above the CDW transition follows neither a Pauli nor a Curie-Weiss paramagnetic behavior. Above 150 K, χ - T seems to evolve in a linear manner, and then a slight downward bending arises and lasts until the CDW transition [Fig. 2(b)]. Similar phenomenon is also observed in other TMDs with CDW transition [28,41–44], which may be attributed to the CDW fluctuation-induced pseudogap above T_{CDW} [45,46].

As shown in Fig. 2(a), a hump-like kink on the ρ - T curve without detectable hysteresis between the cooling and warming cycles occurs at around 43 K, where correspondingly an anomaly in magnetization can also be observed. This anomalous phenomenon is associated with a CDW transition [28] and the T_{CDW} is higher than that of $2H_a$ -NbSe₂ ($T_{CDW} \sim 33$ K). The enhancement of CDW compared to $2H$ -NbSe₂ may be a consequence of enhanced electron-phonon interaction as the case in atomically thin NbSe₂ with reduced

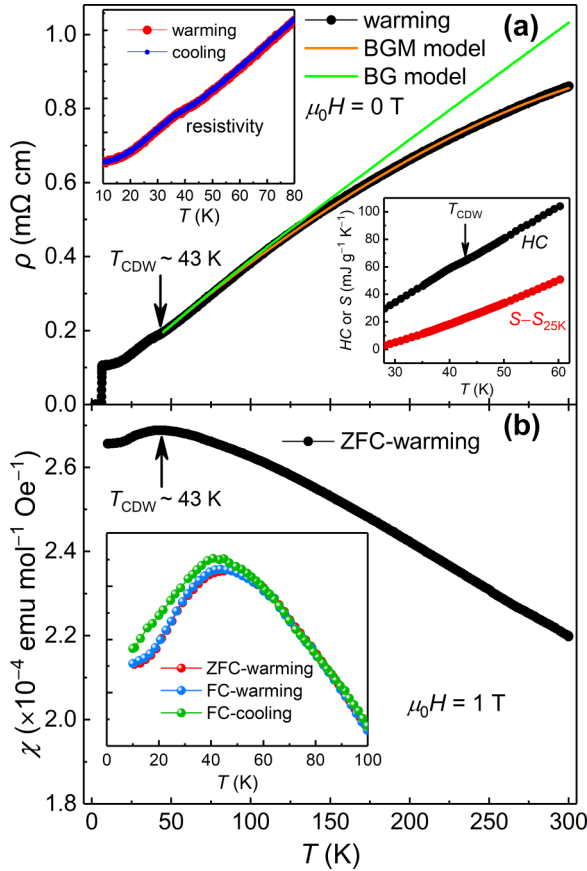


FIG. 2. (a) Temperature-dependent resistivity (ρ) for $4H_a$ -NbSe₂ polycrystalline bulk with $T_{CDW} \sim 43$ K. The green and orange curves, respectively, denote the fitted results from BG and BGM models. The upper inset shows the resistivity from 10 to 80 K measured, respectively, by warming and cooling. The lower inset displays the heat capacity (HC) and entropy (S) around the CDW transition. (b) Temperature-dependent magnetic susceptibility (χ) under zero-field-cooled (ZFC) mode. The inset shows the difference between ZFC-warming, FC-warming, and FC-cooling cycles.

dimensionality [26]. The extremely broadened peak on heat capacity (HC) is frequently observed in CDW system with disorders [47]. This, together with entropy (S) continuity [the inset in Fig. 2(a)] and the absence of thermal hysteresis on ρ - T curve, confirms that it is a second-order CDW transition. The drop in magnetic susceptibility is ascribed to the decrease of DOS-related Pauli susceptibility χ_{Pauli} due to the opening of a CDW gap, from which a change in the DOS of ~ 0.1 eV⁻¹ f.u.⁻¹ (f.u. is formula units) is calculated by the formula $\chi_{Pauli} = \mu_B^2 D(E_F)$. Another interesting observation is that both the zero-field-cooled (ZFC) and field-cooled (FC) magnetizations measured upon warming are nearly coincident, while a small divergence can be observed between the FC-warming and FC-cooling branches below the transition [the inset in Fig. 2(b)]. This weak thermal hysteresis was also observed in CsV₃Sb₅, which indicates a coupling to the lattice [48]. Different from the Ta dichalcogenides in which the CDW transition can be observed obviously in macroscopic measurements, the CDW transition in the NbSe₂ system is weak and extremely susceptible to lattice defects. Because,

in the CDW state, the coupling of electrons and holes at the Fermi surface strongly depends on the lattice vibration, the long-range CDW order is easy to be suppressed by impurities or dislocated by native defects, such as vacancies and stacking faults. During single-crystal growth, the density of the native defects may be increased compared with the well-grown polycrystals, which causes the long-range CDW order to be quenched. This implicitly reflects that EPC may play an important role in the formation of the CDW state in the NbSe₂ system. The phenomenological concurrence of reduced metallicity and decreased DOS around the CDW transition implies that the two phenomena are possibly dominated by the same Fermi surface (FS), while the underlying mechanism is pending clarification in the future. This differs from the case in $2H$ -TaS₂ in which different underlying band structures control the transport and magnetic behaviors. The CDW order in $2H$ -TaS₂ gaps out the FS around the K point but leaves the hole-pocket FS around the Γ point unaffected [49,50]. $4H_a$ -NbSe₂ shows metallic behavior down to 2 K. It is thus rational to suppose that the Fermi surface is partially gapped in the CDW state, and a portion of ungapped, reconstructed FS preserves the metallic conduction. This scenario needs the support from angle-resolved photoemission spectroscopy (ARPES) and optical spectroscopy experiments, etc.

C. Superconductivity

An abrupt superconducting transition emerges in electrical resistivity with onset temperature (T_c^{onset}) at ~ 6.5 K and zero resistivity is reached at ~ 6.2 K [Fig. 3(b)]. The sharp transition with onset at around 6.4 K and 100% diamagnetic shielding signal on the magnetic-susceptibility curve [Fig. 3(a)] demonstrate the bulk superconductivity. T_c of $4H_a$ -NbSe₂ is in line with the previously reported value [29,30] and slightly lower than that of $2H$ -NbSe₂ ($T_c \sim 7.4$ K). ρ - T curves near the transitions measured under various fields from 0 to 16 T are shown in Fig. 3(c); the resistive transition curves shift parallel down to lower temperatures with magnetic fields increasing. The weak magnetoresistance effect allows us to extract the upper critical field H_{c2} by the 90% ρ_n criterion (ρ_n is the normal-state resistivity). $\mu_0 H_{c2}$ as a function of temperature is plotted in Fig. 3(d). Single-band Werthamer–Helfand–Hohenberg (WHH) model incorporates orbital pair breaking and spin-paramagnetic effects in dirty limit [51]. However, the WHH formula could not well describe $\mu_0 H_{c2}(T)$ of $4H_a$ -NbSe₂ when only including the orbital pair breaking [blue solid line in Fig. 3(d)]. Furthermore, the positive curvature near T_c is similar to that observed in MgB₂, YNi₂B₂C, $2H$ -NbSe₂, and $2H$ -NbS₂, reminiscent of a two-band superconductivity in which the different coherence lengths for each band cause the unusual curvature [22,52–54]. We try to fit the experimental data by an effective two-band model [55]:

$$a_0[\ln t + U(h)][\ln t + U(\eta h)] + a_2[\ln t + U(\eta h)] + a_1[\ln t + U(h)] = 0, \quad (2)$$

where a_0 , a_1 , and a_2 are functions of the BCS coupling tensor, $t = T/T_c$; $U(x) = \psi(1/2 + x) - \psi(1/2)$, $\psi(x)$ is the digamma function, diffusivity ratio $\eta = D_2/D_1$; D_1 and D_2 are diffusivities of the two bands; and $h = H_{c2}D_1/2\Phi_0T$, Φ_0 is

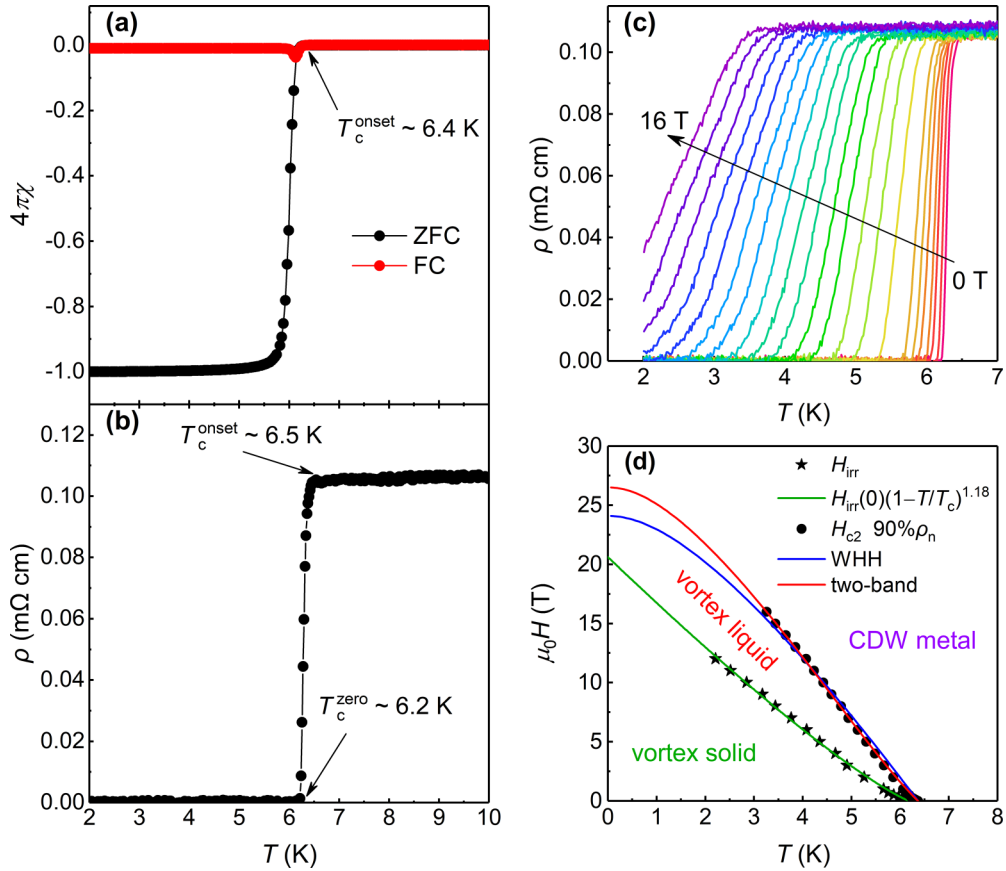


FIG. 3. (a) Superconducting transition in magnetic susceptibility, which shows the onset critical temperature at ~ 6.4 K. (b) Superconducting transition in electrical resistivity with onset and zero-resistivity T_c , respectively, at ~ 6.5 and ~ 6.2 K. (c) Temperature-dependent resistivities near superconducting transitions under various fields from 0 to 16 T. (d) A $\mu_0 H - T$ phase diagram. The irreversible field H_{irr} and upper critical field H_{c2} were obtained by zero-resistivity and 90% ρ_n criteria, respectively. The green solid line represents the fitted result for H_{irr} by the formula $H_{irr}(T) = H_{irr}(0)(1-T/T_c)^{1.18}$. The blue and red lines denote the fitted results for H_{c2} by the WHH and two-band models, respectively.

the magnetic flux quantum $h/2e$. The fitting derives $\mu_0 H_{c2}(0)$ as 26.5 T, which is about 2.25 times the Pauli paramagnetic limit $\mu_0 H_p = 1.84 T_c = 11.8$ T expected for a weak-coupling conventional BCS superconductor, and is much higher than that of $2H_a$ -NbSe₂ in which $\mu_0 H_{c2}(0) \sim 14$ T is comparable to the Pauli limit [56]. The violation of the Pauli limit, a clue to unconventional superconductivity, mostly results from the central inversion symmetry breaking (noncentrosymmetric space group $P-6m2$) which allows for a coexistence of spin-singlet and spin-triplet pairing components, though the possible role of enhanced spin-orbit coupling or increased two dimensionality cannot be ruled out completely. Ginzburg-Landau (GL) coherence length $\xi_{GL}(0)$ was calculated to be 3.5 nm by using the formula

$$\mu_0 H_{c2} = \frac{\Phi_0}{2\pi \xi_{GL}^2}. \quad (3)$$

The irreversible field H_{irr} , the boundary between vortex-solid and vortex-liquid states, was obtained by the zero-resistivity criterion and also plotted in Fig. 3(d). $H_{irr}(T)$ was fitted by a scaling relation $H_{irr}(T) = H_{irr}(0)(1-T/T_c)^{1.18}$, which derives $\mu_0 H_{irr}(0)$ as 20.6 T. This indicates a relatively narrow vortex-liquid region in $4H_a$ -NbSe₂. We note that the search for superconductors with large $\mu_0 H_{c2}(0)$ is of significant im-

portance in high-field magnet applications beyond the widely commercialized NbTi and Nb₃Sn superconductors, but with very slow progress during the past decades. In this respect, to study noncentrosymmetric superconductors that surpass the Pauli limit may open up a path from the structural design strategy to obtain a higher $\mu_0 H_{c2}(0)$.

Lower critical field H_{c1} could provide important information about the bulk thermodynamic properties, such as magnetic penetration depth. Field dependences of isothermal magnetizations ($M-H$) between 0 and 400 Oe measured at different temperatures from 2.0 to 6.4 K are shown in the inset of Fig. 4(a). H_{c1} is defined as the point where the curves begin to deviate from the initial slope and H_{c1} versus T is drawn in the main panel of Fig. 4(a). The curvature change in $H_{c1}(T)$ observed at around 3.5 K may be a characteristic of multiband superconductivity in this system. $H_{c1}(T)$ is given by the following relation [57]:

$$\rho_s(T) = \frac{H_{c1}(T)}{H_{c1}(0)} = 1 + 2 \int_{\Delta}^{\infty} \frac{\partial f(E)}{\partial E} \frac{E}{\sqrt{E^2 - \Delta^2(T)}} dE, \quad (4)$$

where $\rho_s(T)$ is the normalized superfluid density, $f(E)$ is the Fermi function, the BCS-like gap $\Delta(T)$ can be approx-

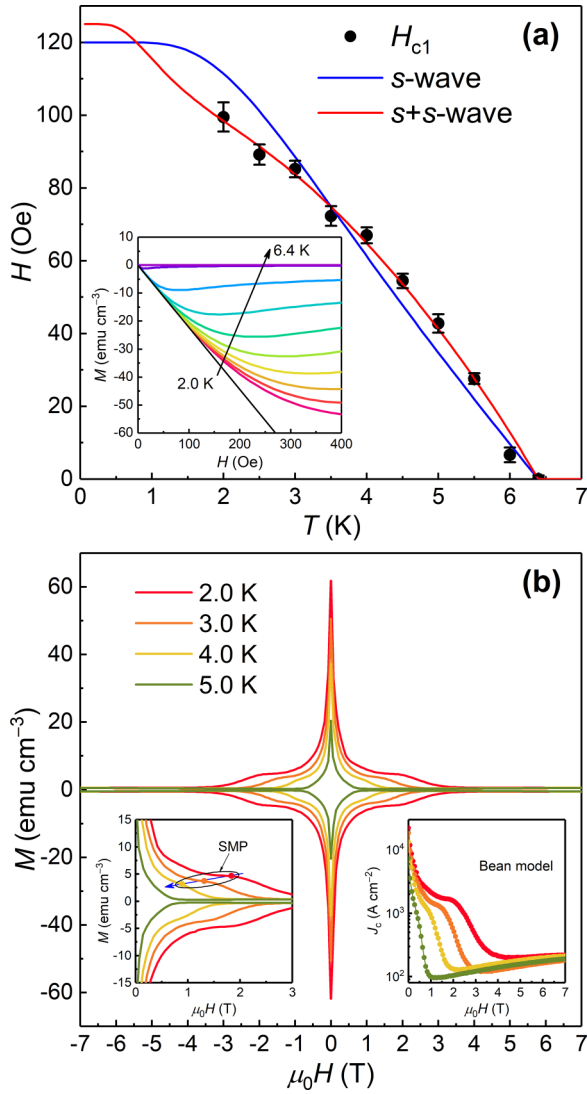


FIG. 4. (a) Lower critical field H_{c1} versus temperature. The blue and red solid lines, respectively, signify the fitted results from the single-gap s -wave and two-gap $s+s$ -wave scenarios. The inset shows the field-dependent magnetizations from 0 to 400 Oe measured at 2.0–6.4 K. (b) Isothermal hysteresis loops at 2.0, 3.0, 4.0, and 5.0 K. The left inset is an enlarged view that indicates the position of SMP and its evolution with temperature. The right inset displays the variations of critical current density (J_c plotted on logarithmic coordinates) with magnetic fields.

imated as $\Delta(T) = \Delta_0 \tanh\{1.82[1.018(T_c/T - 1)]^{0.51}\}$, and $\rho_s(T)$ could be written as $\rho_s(T) = w\rho_s(\Delta_1) + (1-w)\rho_s(\Delta_2)$ with a weighting factor w for the two-gap scenario. $H_{c1}(T)$ fitted by the single-gap s -wave and two-gap $s+s$ -wave models are shown as blue and red solid lines in Fig. 4(a), respectively, revealing that the latter rather than the former gives a better description. This result is in agreement with the μ SR experiment [31]. $H_{c1}(0)$ estimated from the two-gap model is about 125 Oe and the GL penetration depth $\lambda_{GL}(0)$ was calculated as ~ 250.5 nm by the following expression when the Ginzburg-Landau parameter $\kappa_{GL} = \lambda_{GL}/\xi_{GL} \gg 1$ [58]:

$$\mu_0 H_{c1} = \frac{\Phi_0}{4\pi\lambda_{GL}^2} (\ln \kappa_{GL} + 0.49693). \quad (5)$$

$\kappa_{GL}(0)$ was obtained to be $\sim 71.6 (\gg 1/\sqrt{2})$ by assuming that it is T independent, which evidences that $4H_a$ -NbSe₂ is a strong type-II superconductor. Thermodynamic critical field $\mu_0 H_c(0)$ was calculated to be about 261.8 mT by the formula

$$\mu_0 H_c = \mu_0 H_{c2} / \sqrt{2} \kappa_{GL}. \quad (6)$$

The isothermal magnetic hysteresis loop (MHL) of $4H_a$ -NbSe₂ in Fig. 4(b) again confirms that it is a type-II superconductor. Second magnetization peak (SMP) effect induced by the transient relaxation can be seen in the MHL as a fishtail. The peak positions ($\mu_0 H_{SMP} \sim 1.8$ T at 2 K) shift to lower fields with increasing temperature [the left inset in Fig. 4(b)]. Similar SMP with sharp magnetization peak near zero field was also observed in Re₆Zr and some Fe-based superconductors [59,60]. The shape of the MHL and the position of the second peak (well below H_{c2}) are different from those of $2H$ -NbSe₂ [61,62]. This probably points to distinct flux dynamics in the two NbSe₂ polytypes. The symmetric MHL reveals that the bulk pinning rather than the surface barriers dominates the fishtail, while the rapid decay of critical current density $J_c(H)$ with magnetic field demonstrates that it is a system with weak flux pinning. J_c was calculated according to the Bean critical-state model [63]. As illustrated in the right inset of Fig. 4(b), the $J_{c,2K}$ is 2.23×10^4 A cm⁻² under self-field, which quickly decreases to $\sim 7\%$ of $J_{c,2K}(0)$ at 2 T and then increases again above ~ 4.7 T. The reincrease of J_c at all temperatures implies that there may be another SMP at high fields. This is consistent with the high H_{irr} and H_{c2} .

Temperature-dependent specific heat (C) between 1.8 and 10 K under zero field is shown in the inset of Fig. 5(a). A clear specific-heat jump around 6.4 K can be observed, which decisively confirms the bulk nature of the superconductivity. The T_c value determined from the specific-heat measurement is in good agreement with those obtained from the resistivity and magnetization measurements, again evidencing the high quality of the sample. The normal state can be well described by a modified Debye model $C/T = \gamma_n + \beta T^2 + \delta T^4$, where γ_n is the electronic specific-heat coefficient; the second and third terms signify the contributions from the harmonic and anharmonic lattice vibrations, respectively. Fitting the data derives γ_n and β , respectively, as 16.03 mJ mol⁻¹ K⁻² and 0.587 mJ mol⁻¹ K⁻⁴. Debye temperature Θ_D was calculated to be 214.8 K by the formula $\Theta_D = (12\pi^4 n N_A k_B / 5\beta)^{1/3}$, where $n = 3$ is the number of atoms per formula unit. It is instructive to estimate the electron-phonon (e-p) coupling parameter λ_{e-p} to evaluate the e-p interaction in NbSe₂ system. In terms of McMillan's theory for strong-coupled superconductors, λ_{e-p} is given by the following equation from the experimentally determined T_c and Θ_D [64]:

$$\lambda_{e-p} = \frac{1.04 + \mu^* \ln\left(\frac{\Theta_D}{1.45T_c}\right)}{(1 - 0.62\mu^*) \ln\left(\frac{\Theta_D}{1.45T_c}\right) - 1.04}, \quad (7)$$

where μ^* is the repulsive screened Coulomb pseudopotential parameter and taken to be 0.1 as suggested by Refs. [10,65]. Setting $T_c = 7.11$ K, $\Theta_D = 215$ K for $2H$ -NbSe₂ [10] and

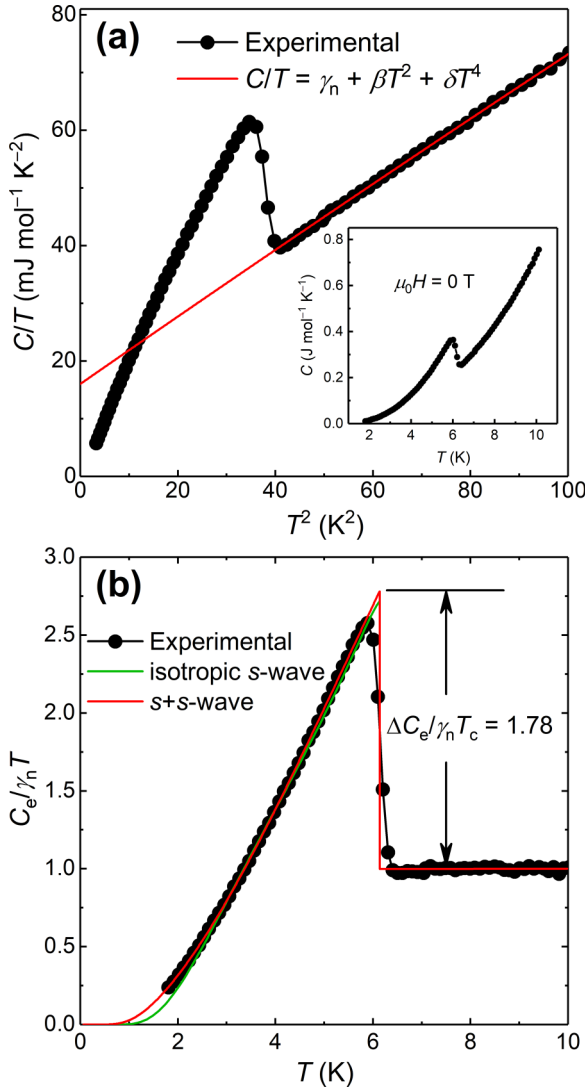


FIG. 5. (a) C/T vs T^2 for $4H_a$ -NbSe₂. The red solid line represents the fitted result from an extended Debye approximation. The inset presents the temperature-dependent specific heat (C) between 1.8 and 10 K, which shows a clear specific-heat jump around the SC transition. (b) The variation of normalized electronic specific heat $C_e/\gamma_n T$ with temperature. The fitted results from the isotropic s -wave and $s+s$ -wave models are displayed as green and red lines, respectively.

$T_c = 6.4$ K, $\Theta_D = 214.8$ K for $4H_a$ -NbSe₂, the λ_{e-p} values are calculated as 0.74 and 0.71, respectively. This indicates an intermediate e-p coupling strength. Thus, the density of states $N(E_F)$ is estimated to be 4.51 and 3.98 eV⁻¹ f.u.⁻¹ for the $2H$ and $4H_a$ phases, respectively, by the formula $N(E_F) = 3\gamma/\pi^2 k_B^2 (1 + \lambda_{e-p})$. This implies that the superconductivity of the NbSe₂ system can be understood in the framework of BCS theory.

The electronic specific heat in the superconducting state is an important probe for gap symmetry. By subtracting the lattice specific heat, the electronic component C_e is obtained and the normalized electronic specific heat $C_e/\gamma_n T$ vs T is shown in Fig. 5(b). The superconducting state $C_{es}(T)/\gamma_n T$ at zero field could be described by the following formula based

on the BCS theory:

$$\frac{C_{es}(T)}{\gamma_n T} = \frac{6}{\pi^2 (k_B T)^3} \int_0^{+\infty} \frac{e^{\sqrt{\varepsilon_k^2 + \Delta_k^2(T)}/k_B T}}{(1 + e^{\sqrt{\varepsilon_k^2 + \Delta_k^2(T)}/k_B T})^2} \times \left(\varepsilon_k^2 + \Delta_k^2(T) - \frac{T}{2} \frac{d\Delta_k^2(T)}{dT} \right) d\varepsilon_k, \quad (8)$$

where $\Delta_k(T) = \Delta(T)g_k(\theta, \phi)$ is a temperature- and angle-dependent gap function, the BCS-like gap $\Delta(T) = \Delta_0 \tanh\{1.82[1.018(T_c/T - 1)]^{0.51}\}$, and $g_k(\theta, \phi) = 1$ for isotropic single s -wave gap. We found that the isotropic single s -wave model could not describe the experimental data well. Thus, we use the two-gap $s+s$ -wave model to analyze the data:

$$\frac{C_{es}(T)}{\gamma_n T} = w \frac{C_{es}^{\Delta_1}(T)}{\gamma_n T} + (1 - w) \frac{C_{es}^{\Delta_2}(T)}{\gamma_n T}, \quad (9)$$

where w is the weighting factor, T_c is defined at 6.13 K to meet the requirement of the entropy balance at the transition, Δ_1 and Δ_2 are derived, respectively, as about 1.20 and 0.40 meV by fitting the experimental data. This provides further evidence for the possible two-gap superconductivity in $4H_a$ -NbSe₂. However, the possibility of an anisotropic single s -wave pairing cannot be ruled out due to the low-dimensional crystal and electronic structures. In this regard, further low-temperature specific-heat, ARPES, and tunneling spectroscopy experiments are of definitive significance. The normalized specific-heat jump $\Delta C_e/\gamma_n T_c$ estimated from the two-gap scenario as 1.78, is larger than the weak-coupling limit BCS value 1.43 but smaller than 2.14 for $2H$ -NbSe₂ [10], which suggests that $4H_a$ -NbSe₂ is a moderately coupled superconductor.

D. *Ab initio* calculations

The calculated energy bands of $2H$ - and $4H_a$ -NbSe₂ without including the spin-orbit coupling effect are shown in Figs. 6(a) and 6(c). A Monkhorst-Pack grid of $17 \times 17 \times 7$ k points was selected to perform the self-consistent calculations and an energy cutoff of 600 eV was used for the wave functions. A denser grid of $25 \times 25 \times 9$ k points was chosen to generate the density of states. Orbital projected bands and DOS are given in Figs. 6(a)–6(d). In both cases, the Nb $4d$ orbits dominate the bands near the Fermi level and the Se $4p$ orbits constitute the valence bands. In addition, some orbits, such as Nb $4d_{xy}$ and $4d_{x^2-y^2}$, Se $4p_y$ and $4p_x$, are degenerate. Hole FS controls the conduction mechanism and multiband character is revealed, in alignment with the Seebeck coefficient [30]. The two materials show almost the same calculated $N(E_F)$, 2.87 eV⁻¹ f.u.⁻¹ for $2H$ -NbSe₂ and 2.91 eV⁻¹ f.u.⁻¹ for $4H_a$ -NbSe₂. According to the BCS theory $T_c = 1.14 \langle \omega \rangle \exp[-1/N(0)V]$, almost the same Θ_D and calculated $N(E_F)$ indicate almost the same T_c . But, the difference in experimental T_c suggests that the CDW may play a role in superconductivity. As shown in Figs. 6(a) and 6(f), $2H$ -NbSe₂ has one Se $4p_z$ -related 3D pancakelike FS pocket centered at the Γ point and two Nb $4d$ -derived ($d_{xy}/d_{x^2-y^2}$) double-walled hole FS sheets surrounding the Γ_A and KH lines, in good agreement with the previous *ab initio* calcu-

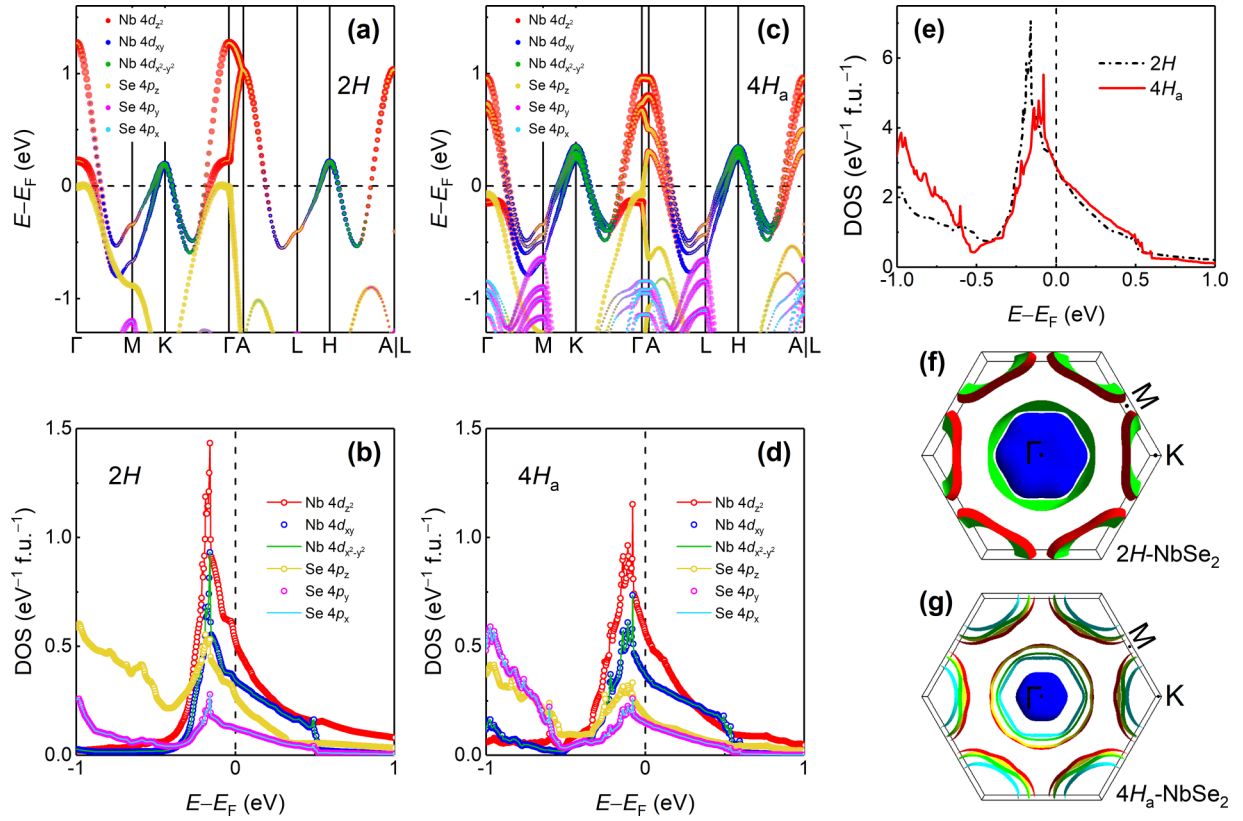


FIG. 6. (a), (c) Calculated energy bands for $2H$ - and $4H_a$ - NbSe_2 projected onto atomic orbitals. (b), (d) Calculated density of states (DOS) projected onto atomic orbitals. (e) Total DOS for $2H$ - and $4H_a$ - NbSe_2 . (f), (g) Fermi surface with high-symmetry points present.

lations and ARPES experiments [66–68]. A superconducting gap was observed at a selected point on the FS sheets around the ΓA line in $2H$ - NbSe_2 by ARPES [68]. In $4H_a$ - NbSe_2 , the number of the Fermi sheets doubles. The Fermi-surface topology of the pocket around the K point remains almost unchanged, still showing strong $d_{xy}/d_{x^2-y^2}$ character. However, the pancake-shaped sheet centered at the Γ point shrinks considerably [Fig. 6(g)]. This indicates that the contribution from the Se $4p_z$ is decreased in the $4H_a$ phase as revealed by DOS more clearly [Figs. 6(b) and 6(d)], implying the weakened p - d hybridization which may account for the reduced T_c compared to the $2H$ polytype. Based on the experimental electronic specific-heat coefficient γ and calculated DOS, the EPC parameters are evaluated as about 1.73 and 1.34 for $2H$ - and $4H_a$ - NbSe_2 , respectively. This seems not to support the higher T_{CDW} in the $4H$ phase from the EPC scenario. From the band dispersion along Γ - K , van Hove singularities (VHSs) can be clearly identified as saddle points in the vicinity of the Fermi level, which could drive the origin of SC and CDW instabilities [69]. The saddle point in $4H_a$ - NbSe_2 is much closer to E_F than that in $2H$ - NbSe_2 . Moreover, the Fermi level E_F of the $4H_a$ phase is also much closer to the VHSs in the density of states compared to the $2H$ phase as illustrated in Fig. 6(e), which may be in favor of the formation of a higher- T_{CDW} CDW order [70]. Stronger CDW and hence lower T_c point to a competition between SC and CDW in the NbSe_2 system. Though the origin of CDW may be different in $4H$ and $2H$ phases, we believe that EPC plays important roles in CDW instability and superconductivity in both

cases, which requires further experimental and theoretical studies.

IV. SUMMARY

In summary, the crystal and electronic structures, and the properties of the CDW transition and SC state of $4H_a$ - NbSe_2 polycrystal were studied systematically. The CDW transition is second order in nature. This type-II BCS superconductor has an intermediate coupling strength and shows SMP effect. The violation of the Pauli limit is mainly caused by the central inversion symmetry breaking. H_{c2} , H_{c1} , and specific heat semiquantitatively support the two-gap $s+s$ -wave pairing scenario. However, strong evidence is needed from measurements at much lower temperatures on single crystals to elucidate the pairing mechanism. The interplay between CDW and SC is a long-standing debated issue. The electronic structures tend to a higher T_{CDW} in $4H_a$ - NbSe_2 . The enhanced CDW and hence suppressed SC compared to $2H$ - NbSe_2 confirm a competitive relation between the two ordered states in NbSe_2 system. This study provides experimental data for understanding SC and CDW, and the interaction between them in TMD compounds. Furthermore, the large upper critical field and the second magnetization peak effect observed in polycrystalline $4H_a$ - NbSe_2 are both favorable for the development of high-field magnets if the superconducting T_c can be further improved, which may also provide an avenue to explore high-field superconductors in noncentrosymmetric materials.

ACKNOWLEDGMENTS

This work was supported by the National Natural Science Foundation of China (Grants No. 12074414 and No. 11774402), the National Key Research and Development

Program of China (Grants No. 2018YFA0704200 and No. 2021YFA1401800), the Strategic Priority Research Program of Chinese Academy of Sciences (Grant No. XDB25000000), and the Excellent Youth Funding of Hunan Provincial Education Department (Grant No. 23B0435).

- [1] Y. D. Wang, W. L. Yao, Z. M. Xin, T. T. Han, Z. G. Wang, L. Chen, C. Cai, Y. Li, and Y. Zhang, *Nat. Commun.* **11**, 4215 (2020).
- [2] B. Sipos, A. F. Kusmartseva, A. Akrap, H. Berger, L. Forró, and E. Tutiš, *Nat. Mater.* **7**, 960 (2008).
- [3] K. T. Law and P. A. Lee, *Proc. Natl. Acad. Sci. USA* **114**, 6996 (2017).
- [4] H. Murayama, Y. Sato, T. Taniguchi, R. Kurihara, X. Z. Xing, W. Huang, S. Kasahara, Y. Kasahara, I. Kimchi, M. Yoshida, Y. Iwasa, Y. Mizukami, T. Shibauchi, M. Konczykowski, and Y. Matsuda, *Phys. Rev. Res.* **2**, 013099 (2020).
- [5] S. Mañas-Valero, B. M. Huddart, T. Lancaster, E. Coronado, and F. L. Pratt, *npj Quantum Mater.* **6**, 69 (2021).
- [6] R. H. Friend, D. Jérôme, R. F. Frindt, A. J. Grant, and A. D. Yoffe, *J. Phys. C: Solid State Phys.* **10**, 1013 (1977).
- [7] J. J. Gao, J. G. Si, X. Luo, J. Yan, Z. Z. Jiang, W. Wang, Y. Y. Han, P. Tong, W. H. Song, X. B. Zhu, Q. J. Li, W. J. Lu, and Y. P. Sun, *Phys. Rev. B* **102**, 075138 (2020).
- [8] A. Ribak, R. M. Skiff, M. Mograbi, P. K. Rout, M. H. Fischer, J. Ruhman, K. Chashka, Y. Dagan, and A. Kanigel, *Sci. Adv.* **6**, eaax9480 (2020).
- [9] I. Guillamón, H. Suderow, J. G. Rodrigo, S. Vieira, P. Rodière, L. Cario, E. Navarro-Moratalla, C. Martí-Gastaldo, and E. Coronado, *New J. Phys.* **13**, 103020 (2011).
- [10] P. Garoche, J. J. Veyssié, P. Manuel, and P. Molinié, *Solid State Commun.* **19**, 455 (1976).
- [11] Y. Deng, Y. M. Lai, X. X. Zhao, X. W. Wang, C. Zhu, K. Huang, C. Zhu, J. D. Zhou, Q. S. Zeng, R. H. Duan, Q. D. Fu, L. X. Kang, Y. Liu, S. J. Pennycook, X. R. Wang, and Z. Liu, *J. Am. Chem. Soc.* **142**, 2948 (2020).
- [12] H. Katzke, P. Tolédano, and W. Depmeier, *Phys. Rev. B* **69**, 134111 (2004).
- [13] Y. Cao, A. Mishchenko, G. L. Yu, E. Khestanova, A. P. Rooney, E. Prestat, A. V. Kretinin, P. Blake, M. B. Shalom, C. Woods, J. Chapman, G. Balakrishnan, I. V. Grigorieva, K. S. Novoselov, B. A. Piot, M. Potemski, K. Watanabe, T. Taniguchi, S. J. Haigh, A. K. Geim, and R. V. Gorbachev, *Nano Lett.* **15**, 4914 (2015).
- [14] T. Jiang, H. T. Wang, H. Gao, Q. H. Zheng, Z. Y. Li, and W. Ren, *arXiv:2210.02922*.
- [15] Y. Nakata, K. Sugawara, R. Shimizu, Y. Okada, P. Han, T. Hitosugi, K. Ueno, T. Sato, and T. Takahashi, *NPG Asia Mater.* **8**, e321 (2016).
- [16] L. W. Liu, H. Yang, Y. T. Huang, X. Song, Q. Z. Zhang, Z. P. Huang, Y. H. Hou, Y. Y. Chen, Z. Q. Xu, T. Zhang, X. Wu, J. T. Sun, Y. Huang, F. W. Zheng, X. B. Li, Y. G. Yao, H. J. Gao, and Y. L. Wang, *Nat. Commun.* **12**, 1978 (2021).
- [17] F. Weber, S. Rosenkranz, J. P. Castellán, R. Osborn, R. Hott, R. Heid, K. P. Bohnen, T. Egami, A. H. Said, and D. Reznik, *Phys. Rev. Lett.* **107**, 107403 (2011).
- [18] T. Valla, A. V. Fedorov, P. D. Johnson, P. A. Glans, C. McGuinness, K. E. Smith, E. Y. Andrei, and H. Berger, *Phys. Rev. Lett.* **92**, 086401 (2004).
- [19] T. Kiss, T. Yokoya, A. Chainani, S. Shin, T. Hanaguri, M. Nohara, and H. Takagi, *Nat. Phys.* **3**, 720 (2007).
- [20] F. Weber, S. Rosenkranz, R. Heid, and A. H. Said, *Phys. Rev. B* **94**, 140504(R) (2016).
- [21] J. D. Fletcher, A. Carrington, P. Diener, P. Rodière, J. P. Brison, R. Prozorov, T. Olheiser, and R. W. Giannetta, *Phys. Rev. Lett.* **98**, 057003 (2007).
- [22] H. Suderow, V. G. Tissen, J. P. Brison, J. L. Martínez, and S. Vieira, *Phys. Rev. Lett.* **95**, 117006 (2005).
- [23] I. Guillamon, H. Suderow, F. Guinea, and S. Vieira, *Phys. Rev. B* **77**, 134505 (2008).
- [24] A. Majumdar, D. VanGennep, J. Brisbois, D. Chareev, A. V. Sadakov, A. S. Usoltsev, M. Mito, A. V. Silhanek, T. Sarkar, A. Hassan, O. Karis, R. Ahuja, and M. Abdel-Hafiez, *Phys. Rev. Mater.* **4**, 084005 (2020).
- [25] E. Oh, G. Gye, and H. W. Yeom, *Phys. Rev. Lett.* **125**, 036804 (2020).
- [26] X. X. Xi, L. Zhao, Z. F. Wang, H. Berger, L. Forró, J. Shan, and K. F. Mak, *Nat. Nanotechnol.* **10**, 765 (2015).
- [27] Y. Xing, K. Zhao, P. J. Shan, F. P. Zheng, Y. W. Zhang, H. L. Fu, Y. Liu, M. L. Tian, C. Y. Xi, H. W. Liu, J. Feng, X. Lin, S. H. Ji, X. Chen, Q. K. Xue, and J. Wang, *Nano Lett.* **17**, 6802 (2017).
- [28] F. J. Di Salvo, J. V. Waszczak, and K. Yamaya, *J. Phys. Chem. Solids* **41**, 1311 (1980).
- [29] I. Naik and S. Sethy, *Curr. Sci.* **114**, 888 (2018).
- [30] I. Naik and A. K. Rastogi, *Pramana-J. Phys.* **76**, 957 (2011).
- [31] F. O. von Rohr, J. C. Orain, R. Khasanov, C. Witteveen, Z. Shermadini, A. Nikitin, J. Chang, A. R. Wieteska, A. N. Pasupathy, M. Z. Hasan, A. Amato, H. Luetkens, Y. J. Uemura, and Z. Guguchia, *Sci. Adv.* **5**, eaav8465 (2019).
- [32] B. H. Toby, *J. Appl. Crystallogr.* **34**, 210 (2001).
- [33] P. Giannozzi, S. Baroni, N. Bonini, M. Calandra, R. Car, C. Cavazzoni, D. Ceresoli, G. L. Chiarotti, M. Cococcioni, I. Dabo, A. D. Corso, S. de Gironcoli, S. Fabris, G. Fratesi, R. Gebauer, U. Gerstmann, C. Gougoussis, A. Kokalj, M. Lazzeri, L. Martin-Samos, N. Marzari, F. Mauri, R. Mazzarello, S. Paolini, A. Pasquarello, L. Paulatto, C. Sbraccia, S. Scandolo, G. Sclauzero, A. P. Seitsonen, A. Smogunov, P. Umari, and R. M. Wentzcovitch, *J. Phys.: Condens. Matter* **21**, 395502 (2009).
- [34] J. P. Perdew, A. Ruzsinszky, G. I. Csonka, O. A. Vydrov, G. E. Scuseria, L. A. Constantin, X. L. Zhou, and K. Burke, *Phys. Rev. Lett.* **100**, 136406 (2008).
- [35] A. D. Corso, *Comput. Mater. Sci.* **95**, 337 (2014).
- [36] J. C. Wildervanck and F. Jellinek, *Z. Anorg. Allg. Chem.* **328**, 309 (1964).
- [37] K. Hayashi, T. Ikeuchi, H. Takeuchi, and M. Shimakawa, *J. Alloys Compd.* **219**, 161 (1995).
- [38] X. C. Li, M. H. Zhou, and C. Dong, *Supercond. Sci. Technol.* **32**, 035001 (2019).

- [39] H. Bai, M. M. Wang, X. H. Yang, Y. P. Li, J. Ma, X. K. Sun, Q. Tao, L. J. Li, and Z. A. Xu, *J. Phys.: Condens. Matter* **30**, 095703 (2018).
- [40] N. F. Mott, *Adv. Phys.* **13**, 325 (1964).
- [41] F. J. Di Salvo, G. W. Hull, Jr., L. H. Schwartz, J. M. Voorhoeve, and J. V. Waszczak, *J. Chem. Phys.* **59**, 1922 (1973).
- [42] X. C. Li, M. H. Zhou, L. H. Yang, and C. Dong, *Supercond. Sci. Technol.* **30**, 125001 (2017).
- [43] M. H. Zhou, X. C. Li, and C. Dong, *Supercond. Sci. Technol.* **31**, 065001 (2018).
- [44] D. Bhoi, S. Khim, W. Nam, B. S. Lee, C. Kim, B. G. Jeon, B. H. Min, S. Park, and K. H. Kim, *Sci. Rep.* **6**, 24068 (2016).
- [45] D. C. Johnston, *Phys. Rev. Lett.* **52**, 2049 (1984).
- [46] J. J. Zhang, D. Phelan, A. S. Botana, Y. S. Chen, H. Zheng, M. Krogstad, S. G. Wang, Y. M. Qiu, J. A. Rodriguez-Rivera, R. Osborn, S. Rosenkranz, M. R. Norman, and J. F. Mitchell, *Nat. Commun.* **11**, 6003 (2020).
- [47] S. Cox, E. Rosten, R. D. McDonald, and J. Singleton, *Phys. Rev. Lett.* **98**, 249701 (2007).
- [48] Q. Chen, D. Chen, W. Schnelle, C. Felser, and B. D. Gaulin, *Phys. Rev. Lett.* **129**, 056401 (2022).
- [49] K. Wijayarathne, J. J. Zhao, C. Malliakas, D. Y. Chung, M. G. Kanatzidis, and U. Chatterjee, *J. Mater. Chem. C* **5**, 11310 (2017).
- [50] W. Z. Hu, G. Li, J. Yan, H. H. Wen, G. Wu, X. H. Chen, and N. L. Wang, *Phys. Rev. B* **76**, 045103 (2007).
- [51] N. R. Werthamer, K. Helfand, and P. C. Hohenberg, *Phys. Rev.* **147**, 295 (1966).
- [52] A. V. Sologubenko, J. Jun, S. M. Kazakov, J. Karpinski, and H. R. Ott, *Phys. Rev. B* **65**, 180505(R) (2002).
- [53] C. L. Huang, J. Y. Lin, C. P. Sun, T. K. Lee, J. D. Kim, E. M. Choi, S. I. Lee, and H. D. Yang, *Phys. Rev. B* **73**, 012502 (2006).
- [54] V. G. Tissen, M. R. Osorio, J. P. Brison, N. M. Nemes, M. García-Hernández, L. Cario, P. Rodière, S. Vieira, and H. Suderow, *Phys. Rev. B* **87**, 134502 (2013).
- [55] A. Gurevich, *Phys. Rev. B* **67**, 184515 (2003).
- [56] S. Foner and E. J. McNiff, Jr., *Phys. Lett. A* **45**, 429 (1973).
- [57] A. Carrington and F. Manzano, *Physica C* **385**, 205 (2003).
- [58] E. H. Brandt, *Phys. Rev. B* **68**, 054506 (2003).
- [59] D. A. Mayoh, J. A. T. Barker, R. P. Singh, G. Balakrishnan, D. M. Paul, and M. R. Lees, *Phys. Rev. B* **96**, 064521 (2017).
- [60] B. Shen, P. Cheng, Z. S. Wang, L. Fang, C. Ren, L. Shan, and H. H. Wen, *Phys. Rev. B* **81**, 014503 (2010).
- [61] D. Pal, S. Ramakrishnan, A. K. Grover, M. J. Higgins, and M. Chandran, *Physica C* **369**, 200 (2002).
- [62] S. S. Banerjee, S. Ramakrishnan, A. K. Grover, G. Ravikumar, P. K. Mishra, V. C. Sahni, C. V. Tomy, G. Balakrishnan, D. M. Paul, P. L. Gammel, D. J. Bishop, E. Bucher, M. J. Higgins, and S. Bhattacharya, *Phys. Rev. B* **62**, 11838 (2000).
- [63] C. P. Bean, *Rev. Mod. Phys.* **36**, 31 (1964).
- [64] W. L. McMillan, *Phys. Rev.* **167**, 331 (1968).
- [65] P. B. Allen and R. C. Dynes, *Phys. Rev. B* **12**, 905 (1975).
- [66] K. Rossnagel, O. Seifarth, L. Kipp, M. Skibowski, D. Voß, P. Krüger, A. Mazur, and J. Pollmann, *Phys. Rev. B* **64**, 235119 (2001).
- [67] F. Weber, R. Hott, R. Heid, L. L. Lev, M. Caputo, T. Schmitt, and V. N. Strocov, *Phys. Rev. B* **97**, 235122 (2018).
- [68] T. Kiss, T. Yokoya, A. Chainani, S. Shin, M. Nohara, and H. Takagi, *Physica B* **312–313**, 666 (2002).
- [69] Y. Hu, X. X. Wu, B. R. Ortiz, S. L. Ju, X. L. Han, J. Z. Ma, N. C. Plumb, M. Radovic, R. Thomale, S. D. Wilson, A. P. Schnyder, and M. Shi, *Nat. Commun.* **13**, 2220 (2022).
- [70] G. H. Li, A. Luican, J. M. B. Lopes dos Santos, A. H. Castro Neto, A. Reina, J. Kong, and E. Y. Andrei, *Nat. Phys.* **6**, 109 (2010).